



Direct numerical simulation of taylor bubble with phase change

Moon Soo Lee^{a,b,*}, Amir Riaz^b

^a Samsung Electronics, 230-0, Giheung-gu, Yongin-si, Gyeonggi-do, Republic of Korea

^b University of Maryland, College Park, MD 20742 USA

ARTICLE INFO

Article history:

Received 7 February 2022

Revised 10 May 2022

Accepted 15 May 2022

Available online 27 May 2022

Keywords:

Flow boiling

Microchannel

Taylor bubble

Heat transfer

Level set method

Direct numerical simulation

ABSTRACT

Direct numerical simulation of evaporating Taylor bubble flow in a vertical cylindrical microchannel is performed. The numerical method for multiphase flow is based on the level set methods with sharp temperature and pressure jump conditions, and diffused interface method with mass flux projection correction scheme for accurate and numerically stable phase change implementation. The numerical method shows good agreement with analytical solutions of adiabatic Taylor bubble flow. Dimensionless parameters: the Reynolds number, the capillary number, the Froude number and the Bond number have been considered in a series of parametric studies to characterize the bubble shape and identify their effects on heat transfer rate enhancement for evaporating Taylor bubble flow.

© 2022 Elsevier Ltd. All rights reserved.

1. Introduction

Multiphase flow in pipes or channels is characterized by specific patterns of the liquid-gas interface that depend on the fluid properties, the mass fraction of the liquid, the heat transfer rate and the flow rate. The regime of slug flow is often found at low vapor qualities where intermittent bodies of liquid and gas phase are formed. A Taylor bubble refers to an elongated bubble, separated by liquid slugs, that almost fills up the tube leaving a thin liquid film on the wall. The basic physical mechanisms related to Taylor bubble flow arise in many fields of engineering research. The study of the well-characterized problem of Taylor bubbles thus enables the understanding of a broad range of the physical phenomenon in practical applications. For example, Horvath et al. [1] found significant improvement in the mass transfer rate in a slug flow through circular tube with immobilized enzyme on the inner wall due to radial mixing. In [2], Oliver and Hoon reported a large enhancement of the heat transfer in slug flow due to radial flow field.

In the application of the Taylor bubble flow for enhanced heat transfer in capillary tubes, both phase changing flow and non-phase changing flow have been considered. A number of studies of heat transfer phenomena in the slug flow regime have revealed that there is a large increase in the wall heat flux and the Nusselt number increases by 1.2 [3] to 6 [4] times that of a pure liquid flow, depending on the operating conditions.

Although both phase changing and non-phase changing Taylor bubble flow have proven to be promising heat transfer technologies in microscale applications, the dominant mechanisms of heat transfer associated with the two modes are different due to the different roles the gas bubble plays. The dominant heat transfer mechanism for non-evaporating or condensing Taylor bubble flow is related to the recirculating flow field in the liquid slug close to the bubble. On the other hand for phase changing flow, whether in a superheated liquid or gas, the phase interface provides a sink at the saturation temperature to remove the heat from the wall. Thus, the gas bubble region and the thin liquid film often play the most critical role in the overall heat transfer and the quick expansion of the gas phase makes the slug to annular flow regime prevalent.

Due to the limitation of experimental methods to measure internal flow and thermal fields in microchannels or tubes, it has been only recently that detailed analyses of the local features of slug flow hydrodynamics and heat transfer characteristics have begun to emerge with the development of accurate direct numerical simulation (DNS) methods for multiphase flow. The numerical studies on non-evaporating or condensing flow have been reported in larger amount compared to studies of phase changing Taylor bubble flow. Fukagata et al. [5] carried out a numerical study on the flow and heat transfer characteristics of a bubble flow train without phase change using the level set method. They were able to obtain qualitative agreement with experimental results regarding wall temperature and found higher local Nusselt numbers beneath the bubble compared to single-phase flow. Narayanan and Lakehal [6] carried out numerical simulations to study the effect of gravity on the two-phase flow heat transfer in small diameter

* Corresponding author at: Samsung Electronics, 230-0, Giheung-gu, Yongin-si, Gyeonggi-do, Republic of Korea.

E-mail address: mslee0523@gmail.com (M.S. Lee).

pipes. They notice that the wall heat transfer of bubbly and slug flow is 3 to 4 times greater than that of pure water flow but the effect of gravity, which increases the bubble breakup frequency, is limited. He et al. [7], using phase field method, studied the heat transfer without phase change in a microtube for slug flow and found that the presence of a gas bubble causes recirculating flow inside the liquid slug, which enhances heat transfer. They found up to 2.4 times higher Nusselt number than that of the single-phase laminar flow. A heat transfer model as a function of parameters such as the slug length, and the flow rate of gas and liquid was proposed assuming negligible gas heat capacity and conductivity, and one-dimensional unsteady heat conduction in liquid film.

Gupta et al. [8] utilized two commercial codes to compare the volume of fluid (VOF) method and the level set method in the study of gas-liquid flows and heat transfer in microchannels with constant wall heat flux and constant wall temperature boundary conditions. They reported around 2.5 times higher Nusselt numbers than for liquid phase flow and claimed that the liquid radial flow at the nose and tail are the basis for enhancement in heat transfer. In their follow-up work [9], validation studies were carried out to substantiate their numerical studies with experiments. The conditions varied for Reynolds numbers in the range 22–1189 and capillary number of 0.003–0.160 with water/nitrogen and ethylene glycol/nitrogen as working fluids. They found close agreement with regard to bubble dynamics and heat transfer rates. They argued that above Reynolds number of about 1000, the flow is no longer axisymmetric.

Sontti and Atta [10] investigated the Taylor bubble behavior in Newtonian and non-Newtonian liquids flowing through a confined co-flow microchannel. The influence of surface tension, inlet velocities, viscosity and concentration of non-Newtonian phase on the bubble on the Taylor bubble characteristics were explored. With increasing carboxymethyl cellulose concentration, bubble formation frequency and velocity increased, but length decreased. A detailed review on the studies of heat transfer with no phase change is presented in Bandara et al. [11].

With regards to numerical studies of slug flow with phase change, Mukherjee and Kandlikar [12] studied a growing water vapor bubble in a microchannel using the level set method. They observed a steady initial bubble growth surrounded by superheated liquid followed by a rapid axial expansion after the bubble fills the channel cross section. The authors also found that the bubble growth rate increased with the liquid superheat and decreased with an increase in the Reynolds number due to a thicker liquid film between the bubble and the wall. Later in Mukherjee [13], Mukherjee et al. [14], they studied nucleating vapor bubble growth in a rectangular microchannel and observed the effect of superheat, surface tension and contact angle. They found that the decrease in the contact angle and increase of wall superheat improves heat transfer while liquid flow rate and surface tension has negligible effect. Zu et al. [15] also numerically investigated bubble nucleation in flow boiling micro-channels using the VOF method implemented in commercial CFD tool, Fluent. The authors compared their results with experimental observations and 1-D theoretical models and found close agreements. Zhuan and Wang [16] performed VOF simulations of flow boiling for R134a and R22 fluids in a 0.5 mm circular channel. These authors analyzed a wide range of flow patterns such as bubbly flow, bubbly/slug flow, slug flow and slug/semi-annular flow depending on bubble evolution as well as the effect of fluid properties on the location of transition lines. The flow patterns and the bubble frequency distribution at the outlet were compared with experimental observations.

Suh et al. [17] used the level set based method with the sharp interface approach to study flow boiling of a bubble in parallel microchannels. They demonstrated that a backward bubble expansion causing reverse flow can occur when the bubble formation is not

simultaneous in the microchannels. They found it to be more pronounced as the contact angle decreases and the wall temperature increases. Magnini et al. [18] used the VOF method in Fluent using the Height Function (HF) approach for improved curvature calculation to simulate a single elongated bubble with phase change in circular microchannels. The authors found that the HF method enhanced the curvature calculation greatly. They reported that the liquid film is the dominant heat transfer mechanism in evaporating slug flow but the heat transfer enhancement due to the bubble wake region is considerable as well. They argued that the main boiling mechanism in the microchannel slug flow cannot be estimated with a conventional nucleate boiling model. A transient-heat-conduction-based boiling heat transfer model for the liquid film region was proposed. Zimmer and Bolotnov [19] studied slug-to-churn vertical two-phase flow regime transition using a finite element based CFD code with level set method implemented. They observed that the bubbles structure during the transition was characterized by instability that grew until they caused breakup of the bubble and the transition initiates when the turbulent film-jet impingement from the wake of the leading bubble reaches the nose of the following bubble. Others have studied liquid film and its heat transfer during vapor bubble expansion in uniformly superheated liquid [20] and bubble condensation in microchannel [21] using VOF method.

Most of above studies used the VOF method and the diffused surface force model [22] which can suffer from inaccuracies in the computation of the surface tension force [23] and mass flux as well as dissipation of interface [16]. Such an approach is susceptible to large errors especially in the case of water in microscale channel because of the large density contrast and high surface tension.

Moreover, we found the detailed understanding of the heat transfer mechanism with respect to various dimensionless parameters in boiling slug flow is still lacking. Phase change can strongly affect bubble fluid dynamics particularly for large Re and large Ca flows where low surface tension force can lead to stronger interfacial instabilities. The current research focuses on the application of highly accurate multiphase flow directly numerical simulation method on systematically identifying the effects of dimensionless parameters, in particular capillary number, Reynolds number, Froude number and Bond number on the heat transfer in Taylor bubble flow with phase change in cylindrical microchannel. The method incorporates the level set methods as the interface capturing method, sharp pressure jump conditions and diffused interface for numerical stability and mass flux projection correction scheme for accurate the phase change phenomenon [24].

2. Models

2.1. Governing equations

Three governing equations: the mass, momentum and energy conservation equations coupled with the interfacial jump conditions are solved to obtain solutions for the pressure, velocity and temperature fields of the Taylor bubble flow domain. There are three interfacial jump conditions: the pressure jump condition due to surface tension force and the phase change, the temperature gradient jump condition due to different thermal conductivity and the velocity jump condition due to the mass transfer and the difference between liquid and gas densities.

Assuming constant specific heat, c and density, ρ within each phase, the energy equation is rewritten in terms of temperature as

$$\rho c \left(\frac{\partial T}{\partial t} + \mathbf{u} \cdot \nabla T \right) = -\nabla \cdot \mathbf{q} + \rho S \quad (1)$$

where ρ is the density, c the heat capacity, T the temperature, t the time, \mathbf{u} the velocity, \mathbf{q} the heat flux, and S the energy source term. The viscous work is considered negligible compared to the convective and conductive heat transfer and no pressure work due to incompressible flow. These assumptions have been common in many literatures concerning incompressible multiphase boiling simulations [25–30]. The heat flux is given by Fourier's law, $\mathbf{q} = -k\nabla T$ where k is the thermal conductivity. The energy source related to the phase change process appears at the phase boundary and is canceled out in this formulation through the Dirichlet interfacial temperature boundary condition, $T_\Gamma = T_{sat}$ where the subscript Γ denotes the interface and Sat the saturation temperature. In other words, all the energy from heat flux across the interface is transformed to evaporation and condensation heat instantly and there is no excess energy left behind.

The mass flux \dot{m} is determined from the heat flux difference across the interface and the latent heat of phase change as

$$\dot{m}_\Gamma = \frac{(-k_l \nabla T_l + k_g \nabla T_g) \cdot \mathbf{n}}{h_{lg}}. \quad (2)$$

The subscripts g and l denote gas and liquid phase respectively, and h_{lg} is the latent heat of evaporation. \mathbf{n} is the interface unit normal which, in current research, is set to points towards the liquid phase.

Then the mass conservation across the interface gives the relation between the mass flux, fluid velocity and the interface velocity by

$$\rho_l (V_\Gamma - \mathbf{u}_l \cdot \mathbf{n}) = \rho_g (V_\Gamma - \mathbf{u}_g \cdot \mathbf{n}) = \dot{m}_\Gamma \quad (3)$$

where V_Γ is the magnitude of the interface velocity in the interfacial normal, \mathbf{n} direction. Reorganizing, the velocity jump condition is given by

$$\mathbf{u}_g - \mathbf{u}_l = \left(\frac{1}{\rho_l} - \frac{1}{\rho_g} \right) \dot{m} \mathbf{n}. \quad (4)$$

The momentum and mass conservation equations are given as

$$\rho \left(\frac{\partial \mathbf{u}}{\partial t} + \mathbf{u} \cdot \nabla \mathbf{u} \right) = -\nabla P + \nabla \cdot \boldsymbol{\tau} + \rho \mathbf{g} \quad (5)$$

$$\nabla \cdot \mathbf{u} = 0. \quad (6)$$

where \mathbf{g} is the body force, in this case the gravity and $\boldsymbol{\tau}$ is the deviatoric stress tensor $\boldsymbol{\tau} = \mu(\nabla \mathbf{u} + (\nabla \mathbf{u})^T)$ where μ is the dynamic viscosity. The thermodynamic properties of the fluids are assumed to be constant within the bulk phases. The surface tension force, the normal tangential stress jump and the mass flux all contribute to the jump in the pressure at the interface as,

$$P_l - P_g = \sigma \kappa + (\mathbf{n} \cdot \boldsymbol{\tau}_l) \cdot \mathbf{n} - (\mathbf{n} \cdot \boldsymbol{\tau}_g) \cdot \mathbf{n} - \left(\frac{1}{\rho_l} - \frac{1}{\rho_g} \right) \dot{m}_\Gamma^2 \quad (7)$$

where κ is the curvature and σ is the surface tension coefficient. In current research, κ is negative for circular gas bubble interface because the interface normal points towards the liquid phase. The surface tension coefficient is assumed to take on a constant value corresponding to the saturation temperature. Also, the normal stress jump term is treated by smoothing the viscosity across the interface.

2.2. Interface velocity and advection

The interface, Γ is represented using the level set method [31,32] and is given by

$$\Gamma(t) = \{\mathbf{x} \in \Omega : \phi(\mathbf{x}, t) = 0\} \quad (8)$$

$$\phi(\mathbf{x}, t) = \pm |\mathbf{d}|, \quad (9)$$

where the level set function ϕ is defined as the signed distance to the closest zero level set. The signs naturally correspond to two different phases, in current cases, gas ($\phi < 0$) and liquid ($\phi > 0$). The advection of the level set function is performed by

$$\frac{\partial \phi}{\partial t} + \mathbf{u}_\Gamma \cdot \nabla \phi = 0. \quad (10)$$

The interface velocity field is calculated from reorganizing Eq. (3) in terms of \mathbf{u}_Γ as,

$$\begin{aligned} \mathbf{u}_\Gamma &= V_\Gamma \mathbf{n} + [\mathbf{u}_l - (\mathbf{u}_l \cdot \mathbf{n}) \mathbf{n}] = \frac{\dot{m} \mathbf{n}}{\rho_l} + \mathbf{u}_l \\ &= V_\Gamma \mathbf{n} + [\mathbf{u}_g - (\mathbf{u}_g \cdot \mathbf{n}) \mathbf{n}] = \frac{\dot{m} \mathbf{n}}{\rho_g} + \mathbf{u}_g \end{aligned} \quad (11)$$

Because the interface, ϕ is an implicit representation, it is important to construct a smooth and uniform magnitude interface velocity field around the phase interface in order to advect ϕ according to Eq. (10). While the construction of \mathbf{u}_Γ through Eq. (11) is continuous at the interface, it is not necessarily divergence free nor smooth, and simple mass source diffusion can results in a large error in mass conservation. Current study incorporates a novel diffused interface approach using the ghost fluid technique and mass flux projection correction scheme to avoid such error while keeping the sharp, ghost fluid treatment for all jump conditions. More details of the current numerical method can be found in Lee et al. [24].

2.3. Dimensionless parameters and non-dimensionalization

The dimensionless parameters that define the governing equations of the current study are the capillary number, Reynold number, Froude number, Stefan number and Prantl number. They are defined as follow:

$$\begin{aligned} Ca_b &= \frac{\mu_l U_{tb}}{\sigma} \\ Re &= \frac{\rho_l U_{sl} D}{\mu_l} \\ Fr &= \frac{U_{sl}}{\sqrt{gD}} \\ St &= \frac{C_{p,l}(T_{wall} - T_{sat})}{h_{gl}} \\ Pr &= \frac{\mu_l C_{p,l}}{k_l} \end{aligned} \quad (12)$$

where the scaling factors D , U_{sl} and U_{tb} are tube diameter, the superficial liquid inlet velocity and the bubble tip velocity, respectively.

σ is the liquid-gas surface tension, ρ the density, μ the viscosity, g the gravitational acceleration, C_p the heat capacity, h_{gl} the latent heat and k the thermal conductivity. The velocity, length, time and pressure in the governing equations are non-dimensionalized using U_{sl} , D , D/U_{sl} and $\rho_l U_{sl}^2$, respectively. For superheated liquid evaporating condition, the temperature is normalized as

$$T' = \frac{T - T_{sat}}{T_{wall} - T_{sat}}. \quad (13)$$

and the heat transfer rate on the wall can be described with the local Nusselt number as

$$Nu = \frac{D}{(T_{wall} - T_{sat})} \frac{\partial T}{\partial r} \Big|_{r=D/2} \quad (14)$$

and with the mean Nusselt number as

$$\overline{Nu} = \frac{1}{L_d} \int_0^{L_d} Nu \, dx \quad (15)$$

where T_{wall} and T_{sat} is the wall temperature and the saturation temperature, respectively.

The governing equations, fluid properties and the transport variables are non-dimensionalized primarily based on the liquid phase and the gas-liquid ratios are used to write the gas phase equations. The liquid and gas phase Navier–Stokes equation are given in dimensionless form as

$$\frac{\partial \mathbf{u}}{\partial t} + \mathbf{u} \cdot \nabla \mathbf{u} = -\nabla P + \nabla \cdot \left[\frac{1}{\text{Re}} (\nabla \mathbf{u} + (\nabla \mathbf{u})^T) \right] + \frac{1}{\text{Fr}^2} \hat{\mathbf{k}} \quad (16)$$

$$\frac{\partial \mathbf{u}}{\partial t} + \mathbf{u} \cdot \nabla \mathbf{u} = -\frac{1}{\rho'} \nabla P + \nabla \cdot \left[\frac{\mu'}{\rho'} \frac{1}{\text{Re}} (\nabla \mathbf{u} + (\nabla \mathbf{u})^T) \right] + \frac{1}{\text{Fr}^2} \hat{\mathbf{k}} \quad (17)$$

where $\rho' = \rho_g/\rho_l$ and $\mu' = \mu_g/\mu_l$. For the temperature equation, they are

$$\frac{\partial T}{\partial t} + \mathbf{u} \cdot \nabla T = \nabla \cdot \left(\frac{1}{\text{RePr}} \nabla T \right) \quad (18)$$

$$\frac{\partial T}{\partial t} + \mathbf{u} \cdot \nabla T = \nabla \cdot \left(\frac{\alpha'}{\text{RePr}} \nabla T \right) \quad (19)$$

where $\alpha' = \alpha_g/\alpha_l$ is the thermal diffusivity ratio. The notion ' for the dimensionless transport variables is omitted. The mass flux is expressed with the Stefan number and the Peclet number as,

$$\dot{m}_\Gamma = -\frac{\text{St}}{\text{RePr}} k' \nabla T_g \cdot \mathbf{n} + \frac{\text{St}}{\text{RePr}} \nabla T_l \cdot \mathbf{n} \quad (20)$$

and the pressure jump

$$P_l - P_g = \frac{\kappa}{\text{We}} - \left(\frac{1}{\rho'} - 1 \right) \dot{m}_\Gamma^2 \quad (21)$$

where We is the Weber number defined as $\text{We} = \frac{\rho_l U_{sl}^2 D}{\sigma}$.

2.4. Computational domain

The current research aims to study the heat transfer phenomena for the evaporating Taylor bubble flow in a vertical tube with constant wall temperature. There are two main types of computational domain that have been commonly used to study the Taylor bubble flow: the moving frame and the fixed frame of reference. The moving frame of reference, where the computational domain follows the bubble, requires a much smaller number of meshes which lowers the computational cost. It is thus suitable for studying steady or quasi-steady dynamics of a single bubble. Also, it allows the researcher to easily control the bubble and liquid slug length ratio if the focus is on the homogeneous void fraction effect on the flow or heat transfer characteristics. On the other hand, a fixed frame domain typically includes a junction or a nozzle at the inlet region and has been utilized to study the entrance effect such as the liquid-gas inlet mass flux ratio on the periodic release of bubbles.

A moving frame of reference is used for the current research in order to efficiently study the long-term behaviors of evaporating Taylor bubble as well as a wide range of dimensionless parameters where the length scale and the time scale can differ by orders of magnitude. There are a few approaches to implement the moving computational domain. One of them is by moving the wall in opposite direction of the bubble advancement [33,34]. Others have used dynamic mesh moving with the bubble advancement [35]. The authors have used the first method of moving the wall, which is simpler to implement but assumes that the flow is fully developed at the upstream and downstream boundaries. The moving wall boundary condition is applied in which the bubble tip velocity U_{tb} is used to update the moving wall velocity U_{wall} at each time step as

$$U_{wall}|_{r=R/2} = -U_{tb} \quad (22)$$

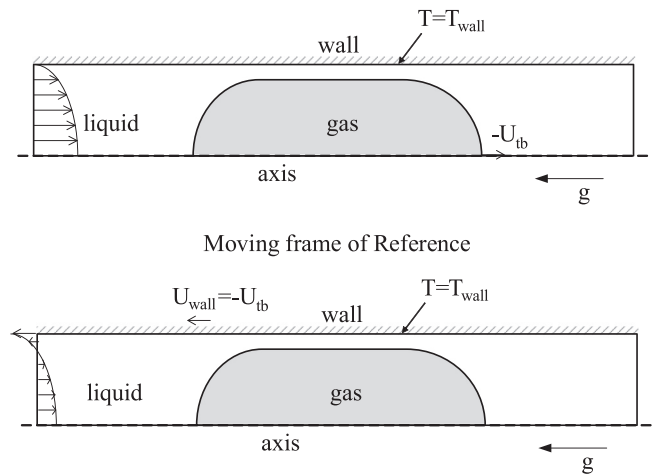


Fig. 1. Schematic of computational domain for Taylor bubble flow. (Top) Fixed framed and (Bottom) moving frame of reference.

and the inlet velocity as

$$U_{in} = U_{sl} + U_{wall} \quad (23)$$

where U_{in} is the updated velocity inlet boundary condition.

By linearly transforming the velocity boundary conditions at the wall and at the inlet with the bubble velocity in the opposite direction $-U_{tb}$, the momentum and mass conservation equations solves for a solution field $\mathbf{u}_{solution}$ in a reference frame that is moving along with the bubble. In other words, to look at the velocity field in the fixed frame of reference (as we would see standing still), we must transform the x -direction velocity as $u_{x,solution} + U_{tb}$. Similarly, the temperature field is solved within the moving reference frame where the wall and at the inlet velocity are observed to be moving at $-U_{tb}$. Thus, the convective term in the heat transfer equation is solved using the same velocity field solution in the moving frame of reference. The level set function is also updated in moving frame of reference, such that the bubble stays in the computational domain. The temperature boundary condition at the inlet and outlet is the Neumann boundary condition. Thus, thermal boundary layer at the wall entering or exiting at the inlet and the outlet is assumed to be linearly continuous. This assumption implies that for inlet and outlet boundaries distant far enough from the bubble would simply be developing at the same rate in the liquid slug region. It should be stressed that current research does not use periodic boundary condition but assumes an isolated bubble behavior. The periodic boundary condition is not easily applicable to heat transfer studies because the energy flow is not the same at the inlet and the outlet. The temperature field initial condition is setup at the saturation temperature for both liquid and gas, while the wall temperature is at a higher constant temperature. Fig. 1 shows a schematic of the computational domain used here.

The moving axisymmetric computational domain of the circular tube has a diameter of D and the length is $L_d = 8D$. The bubble is initially placed at the center of the computational domain thus the bubble entrance effect is not considered in current simulations. The model assumes that there is no nucleation point other than on the surface of the bubble initially places at the center of the computational domain. Also, liquid dry out at the wall is not considered. This assumption is in accordance with other researcher's finding that wall dry out is only observed under particular conditions and not likely in an isolated Taylor bubble case in circular micro-channel tube as in current research cases [23].

Also, a single evaporating bubble is taken into account by assuming that neighboring bubbles are far and interference effects are negligible. Due to phase change, the solution is transient in

Table 1
Properties of nitrogen and ethylene glycol at 294.15 K.

Phase	ρ [kg/m ³]	μ [μ Pa s]	C_p [J/kg K]	k [W/mK]	σ [N/m]
Nitrogen	1.126	21.2	1040	0.0242	0.048
Ethylene glycol	1107	14,000	2627	0.2510	

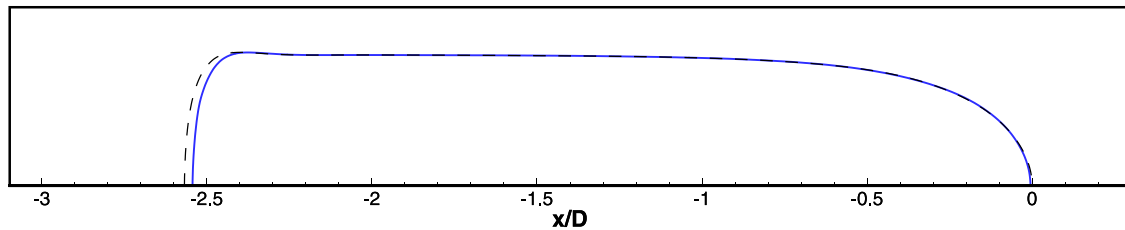


Fig. 2. Shape of the bubble for validation case with two grid resolutions (dashed line for 60×960 and solid line for 120×1920) at $t = 2$.

nature and the bubble growth from about $1.74D$ to $4D$ has been considered in the current study. The initial bubble shape is a spherocylinder with a hemispherical cap at each end. The initial bubble length is $4R_b$ and the bubble radius is $R_b = 2/3D$. The radius is defined roughly based on the prediction of liquid film thickness because although the quasi-steady bubble shape is independent of the initial setup, closer initialization can reduce the computational time to reach it.

As mentioned, the inlet boundary condition is set with the inlet velocity U_{in} which varies in time together with the moving wall velocity. Axisymmetric boundary condition is used at $r = 0$ and a zero pressure boundary condition at the outlet.

2.5. Validation with adiabatic Taylor bubble flow in vertical tube

Simulations of a Taylor bubble flow under isothermal condition has been carried out to validate our numerical method as well as to estimate the required grid resolution for various cases. The adiabatic Taylor bubble flow has been studied extensively by means of experiments and DNS multiphase numerical methods. Quite a number of predictive models have been developed that estimate the hydrodynamics of the Taylor bubble flow such as the thickness of the liquid film around the bubble δ , bubble rise velocity U_{tb} and pressure drop, and will be discussed with our results.

The validation conditions have been set up as one of the cases in the work of Gupta [9] where both experimental and numerical studies were performed. The properties of the gas and liquid phases are that of nitrogen and ethylene glycol at 294.15 K (Table 1). In a tube of radius 0.002 m, the velocity of the superficially flowing liquid phase, U_{sl} is 0.37 m/s. The grid convergence is tested in Fig. 2 with a 60×960 mesh and a mesh twice as fine. x/D is the normalized distance from the bubble front tip and does not reflect the distance traveled by the bubble. The comparison shows a close match with a small deviation of the bubble tail location but an exact match for the bubble thickness and the interface profile. Thus the mesh 60×960 has been used throughout the current research. Note that for a research aimed towards turbulent features of the Taylor bubble flow as in Zimmer and Bolotnov [19], a finer mesh is required as the bubble shape develops greater instability.

Bretherton [36] provided a theoretical work based on the lubrication approximation and predicted the liquid film thickness between the bubble and the wall to be

$$\delta/R = Ca_b^{2/3}. \quad (24)$$

However, it was later found that the film thickness only obeys Taylor's law at a small capillary number ($Ca < 0.03$). A more accurate

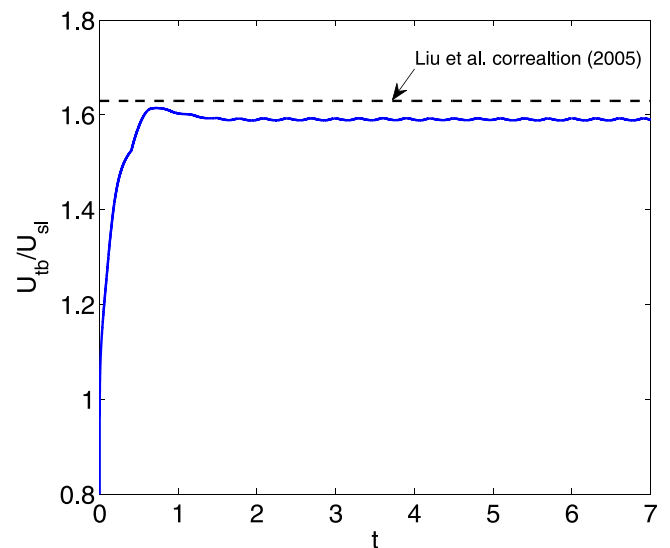


Fig. 3. Normalized bubble tip velocity as a function of time for the validation case.

correlation was proposed later by Aussillous and Quere [37] as

$$\delta/R = \frac{1.34Ca_b^{2/3}}{1 + 1.34 \times 2.5Ca_b^{2/3}}. \quad (25)$$

where the coefficient 2.5 is empirical. This correlation has been widely used for low Reynold number, $22 < Re < 40$. The thickness obtained from the numerical simulation was $\delta/R = 0.20156$ and the correlation result is 0.2015 while the experimental values from matching capillary number, shown in Fig. 6 of [9], were approximately between 0.21 and 0.22. A prediction of bubble terminal velocity is given by Liu et al. [38] for upward Taylor flow in vertical channels as

$$U_{tb}/U_{sl} = \frac{1}{1 - 0.61Ca_b^{0.33}}. \quad (26)$$

This correlation has been shown to be valid for Ca in the range of 0.0002–0.39. Fig. 3 shows the bubble rising velocity in time and the result of the validation case is in close agreement with the correlation.

In two-phase slug flow, the pressure drop increases due to the circulating flow field and the increase of shear stress at the wall. In the liquid slug, the pressure drop is consistent with Hagen–Poiseuille flow and the shear of the gas phase is negligible within the liquid film region. However, the pressure drop over the entire bubble, ΔP_{bubble} , is not zero because the pressure jump at the bub-

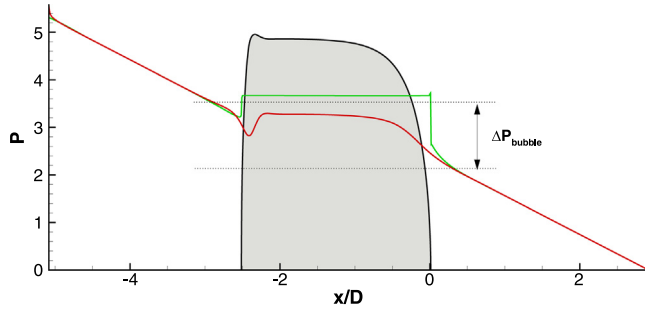


Fig. 4. Pressure drop in the tube and sharp pressure jump inside the bubble along the tube center (red) and the wall (green) at $t = 2$. (For interpretation of the references to color in this figure legend, the reader is referred to the web version of this article.)

ble front is larger than the back. The pressure drop over the computational domain is thus the sum of the liquid slug pressure drop and the bubble pressure drop. A pressure drop correlation is given by Kreutzer et al. [39] as

$$\frac{\Delta P}{L_{uc}} = \frac{16}{\text{Re}} \left[1 + a \frac{D}{L_s} \left(\frac{\text{Re}}{\text{Ca}} \right)^{(1/3)} \right] \frac{4}{D} \left(\frac{\rho_l U_{in}^2}{2} \right) \vartheta_l \quad (27)$$

where L_s is the liquid slug length, ϑ_l is the dynamic liquid hold-up and a is found to be 0.07 for the numerical and 0.17 for the experimental result. Pressure field along the tube center and the wall is plotted for the current simulation in Fig. 4 at $t = 2$. The above correlation gives the normalized pressure drop over the computational domain as 5.635 which is close to the current simulation result of 5.321. It also shows that the pressure drop along the tube center and the wall is linear in the liquid slug region whereas there is a sharp jump in the gas phase due to surface tension force. The wall pressure is shown to increase largely at the bubble front and then drops with fluctuation at the rear of the bubble. Similar observations were found in Gupta et al. [23], Kreutzer et al. [39].

2.6. Results and discussion

2.6.1. Reference case

A reference case for the Taylor bubble with phase change is setup with: $\rho_g/\rho_l = 0.01$, $\mu_g/\mu_l = 0.01$, $k_g/k_l = 0.02$, $C_{p,g}/C_{p,l} = 0.33$ and the dimensionless numbers are given as: $\text{Ca} = 0.033$, $\text{Re} = 125$, $\text{Fr} = 2.52$ and $\text{St} = 0.003$. The length scale corresponds to $D = 0.001$ m tube diameter and the velocity is scaled with inlet liquid velocity U_{sl} since the bubble tip velocity U_{tb} does not asymptote to a constant value in the phase changing flow cases. The properties and the reference scales are varied individually from the reference case to isolate the effects of each dimensionless parameter.

The reference case is depicted in Fig. 5, where the bubble growth from the initial shape is shown over a time interval of about 2. Here, the bubble quickly forms a stable profile after which the front and the tail shapes are not affected by the growth. Also, the growth rate increases due to an increase in the surface area available for evaporation. In Fig. 6 (Top), the normalized bubble tip

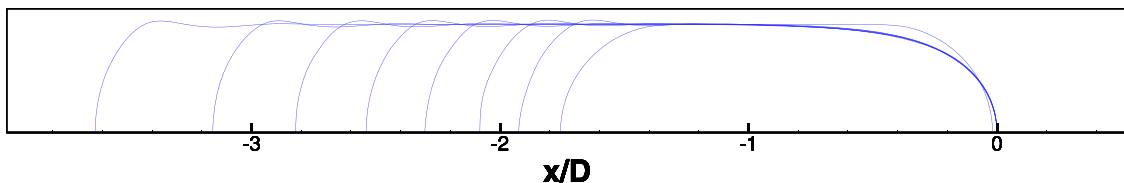


Fig. 5. Bubble growing due to evaporation for the reference case. The snap shots are taken at intervals of $\Delta t = 2$.

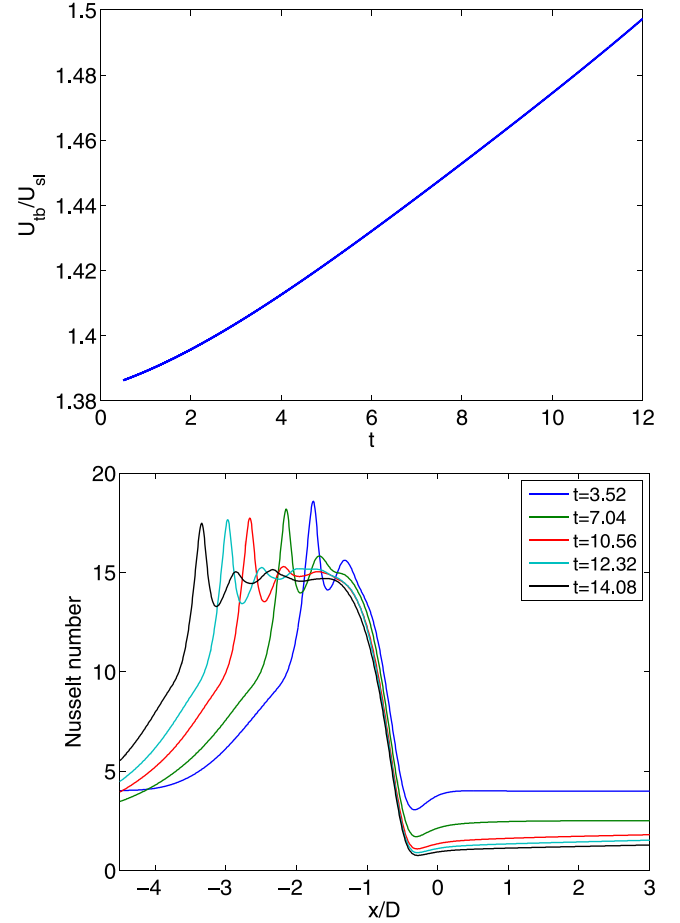


Fig. 6. (Top) Normalized bubble tip velocity as a function of time and (Bottom) local Nusselt number evolution in time for the reference case.

velocity is plotted as a function of time. The bubble tip velocity continuously grows within the computational time due to an increase in the surface area of evaporation and the buoyancy force. In Fig. 6 (Bottom), the local Nusselt number and its development in time is shown. It can be seen that the major heat transfer occurs due to the thin liquid film region and that the characteristic profiles of the Nusselt number are almost identical during the bubble growth with a slight decrease due to the thermal boundary development.

The fluctuation of the film thickness at the rear of the bubble is due to the balance between surface tension and the thin film related momentum flux. The lowest pressure at the exit of the liquid film shown in Fig. 7 (Top) contributes to the highest crest at the tail. Fig. 6 shows that the maximum wall heat flux at the rear cap of the Taylor bubble as well as smaller fluctuations along the film region to be more amplified than the interface profile. It is found that the location of the trough and the crest of the Nusselt number wave closely match the boundaries and the center of the adjacent vortices shown in Fig. 7 (Middle) where the axial veloc-

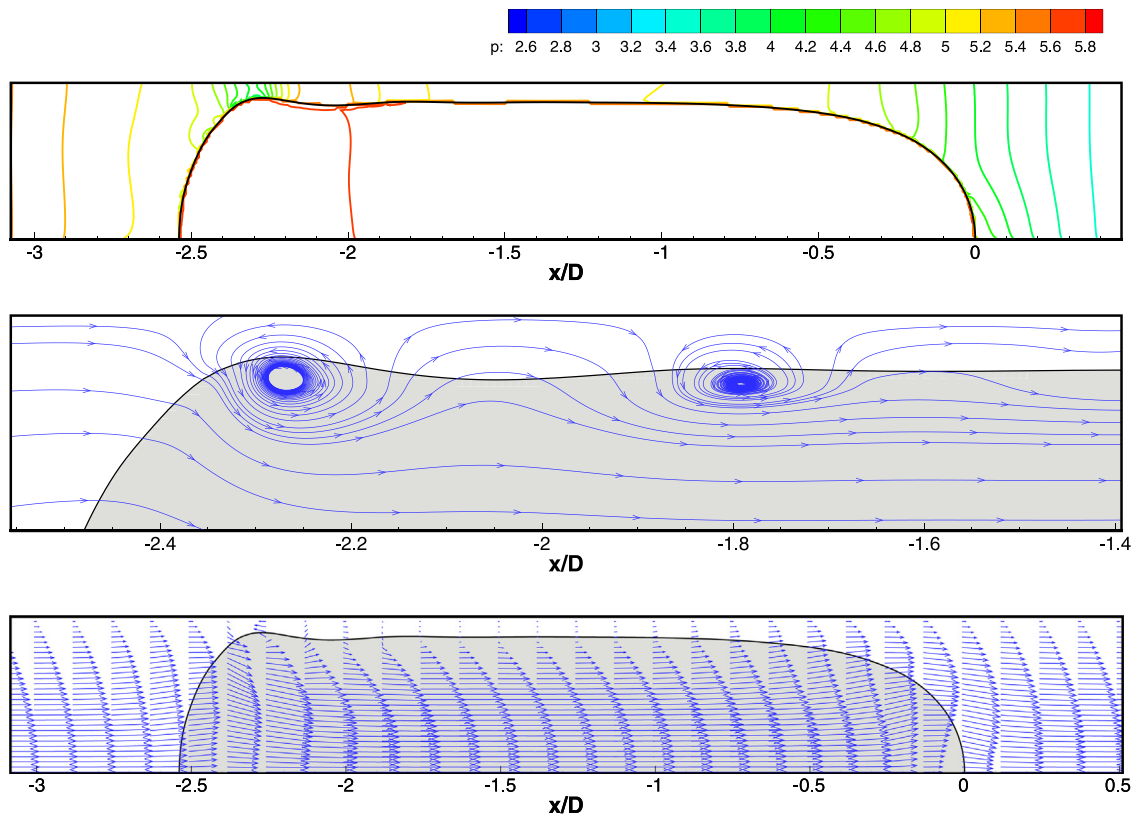


Fig. 7. (Top) Pressure contours around the reference bubble, (Middle) Recirculating flow near the tail of the reference bubble and (Bottom) Fluid velocity field of the reference bubble at $t = 8$.

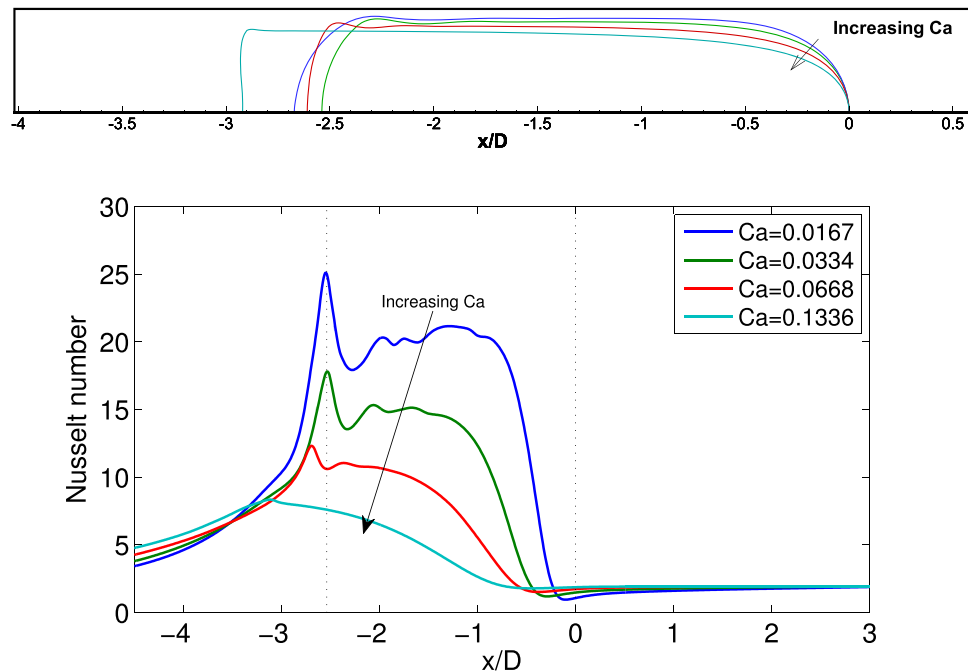


Fig. 8. Comparison of (Top) bubble shape and (Bottom) local Nusselt number distribution within the moving frame of reference for varying capillary numbers in the range of 0.0167–0.1336. The time is at $t = 8$. Dotted lines show the front and rear of the reference case bubble.

ity is lowest and highest respectively. Similar observations were reported in Gupta et al. [8], Lakehal et al. [40]. In Fig. 7 (Bottom), the fluid velocity field of the reference bubble is shown. Here, it can be seen that the velocity inside the bubble is faster and the velocity at the constant film thickness region is almost stagnant. Thus, the

gas phase is flowing effectively at a smaller diameter due to the liquid film.

2.6.2. Parametric studies

Results of the parametric study involving capillary number, Reynolds number and Froude number in phase changing Taylor

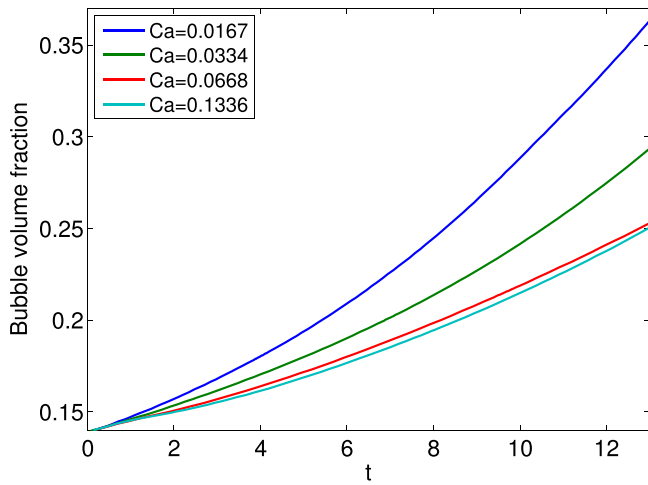


Fig. 9. Bubble growth rate for varying Ca . The bubble volume fraction is in reference to the computational domain.

bubble flow are discussed starting with the influence of the capillary number. According to Eqs. (24) and (25), it is the primary parameter that determines the liquid film thickness concerning microchannel flows.

In Fig. 8 (Top), the shapes of the bubble in varying capillary numbers are shown. As expected, a monotonic increase in the liquid film thickness is observed as the capillary number increases. The interface profiles of the bubble front are smooth for all capillary numbers whereas the profiles at the tail are wavy and transient. A flatter bubble tail can be found as the capillary number increases and at the highest Ca of 0.1336, the liquid film thickness decreases from the front to the tail almost linearly without a typical peak region.

The effect of the capillary number on the local Nusselt number distribution at $t = 8$ is plotted in Fig. 8 (Bottom). First, it shows a decrease in the Nusselt number as the capillary number increases in accordance with the thickening of the liquid film and lower temperature gradient at the wall. As the film gets thicker, the Nusselt number fluctuations decrease and almost vanish for the highest Ca . Comparison of the bubble growth over time for the varying Ca cases is plotted in Fig. 9. The lower capillary number exhibits a faster growth rate because the bubble growth rate depends on the total heat flux at the gas-liquid interface. Assuming linear thermal gradient within the liquid film, it would largely depend on the film thickness. Note that the area of the liquid film region may be larger for higher Ca number bubbles due to elongated shape but it can be seen that its effect is negligible.

In Fig. 10 (Top), the profiles of the bubbles are drawn for varying Re . The bubble front shape slims monotonically in response to the Reynolds number increase. Near the tail of the bubble, however, the liquid film develops a wavy profile. The waviness of the film seems to increase until about $Re = 375$ and then decrease thereafter. Also, the shape of the bubble tail changes from a hemispherical shape to a flat shape and then to a concave shape as Re is increased further. This is due to a relative decrease in surface tension force and stronger transient recirculation regions in the bubble wake as well as inside the bubble. For $Re > 375$, the wavy profile and the flattened bubble tail begin to show quasi-steady-state oscillation.

Fig. 10 (Bottom) shows the effect of Reynolds number on the local Nusselt number distribution. At low Reynolds numbers (< 125), the Nusselt number profile varies little in shape showing a decrease at the front of the bubble and a larger peak at the bubble tail as Re is increased. The increase in peak corresponds to the increase in wavy profile at the tail and occurs due to the contribution of higher velocity and larger vortex near the tail inducing a thinner gap between the bubble and the tube. When the Reynolds number is further increased, the slope of Nusselt number jump

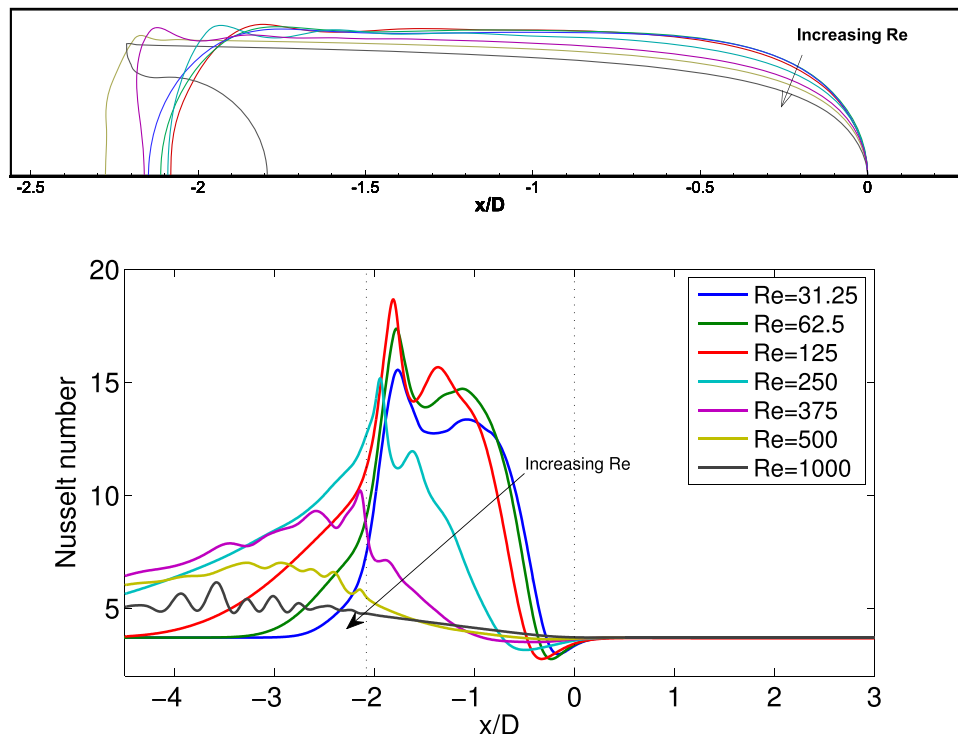


Fig. 10. (Top) Bubble shape with respect to the time scale of the reference case, $Re = 125$ and (Bottom) local Nusselt number distribution within the moving frame of reference with Reynolds number varying in the range of 31.25–1000. The time is at $t = 4$ with respect to the time scale of the reference case, $Re = 125$. Dotted lines show the front and rear of the reference case bubble.

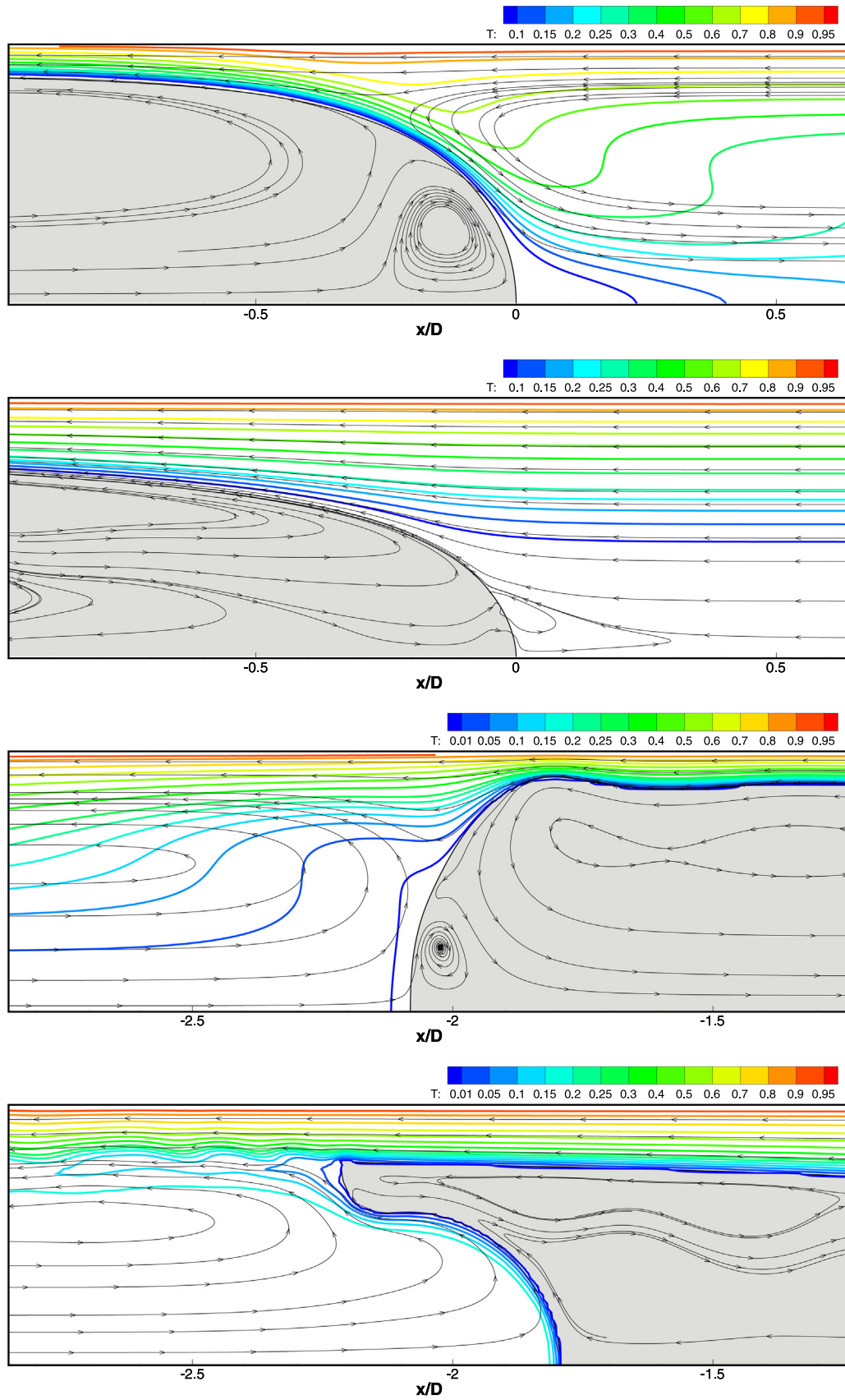


Fig. 11. Temperature profiles near front and near tail of the bubble for the reference case (top and third) and $Re = 1000$ (Second and bottom). The streamlines are based on the velocity relative to the moving frame of reference.

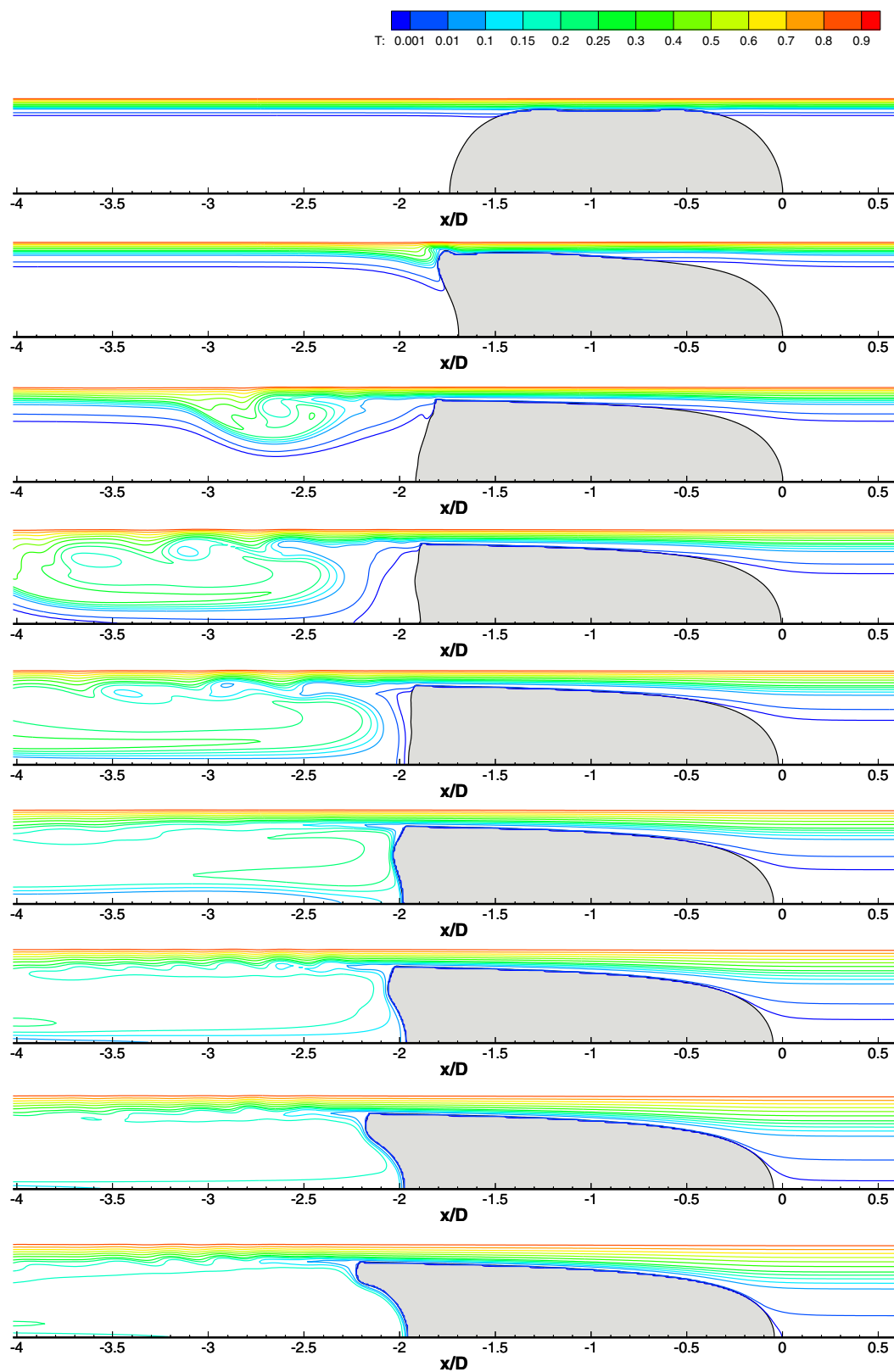


Fig. 12. Time evolution of the bubble shape and the temperature contour for $Re = 1000$.

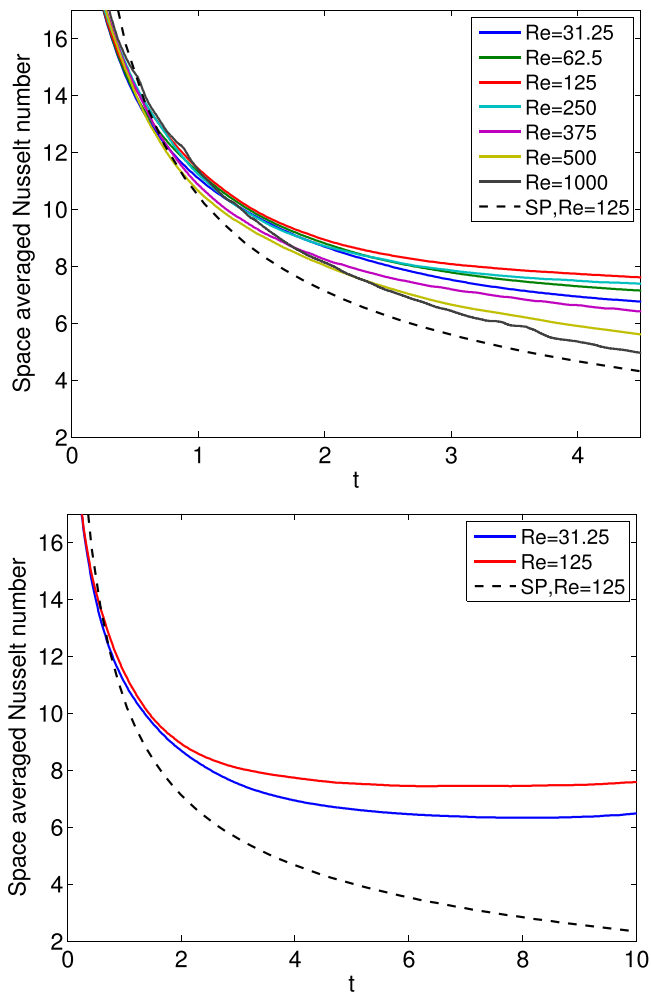


Fig. 13. (Top) Space averaged Nusselt number evolution in time for varying Re. (Bottom) Long term behavior of the space averaged Nusselt number in time. Dotted line is the pure liquid phase with constant T_{wall} condition and the domain is moving at the speed of the reference bubble.

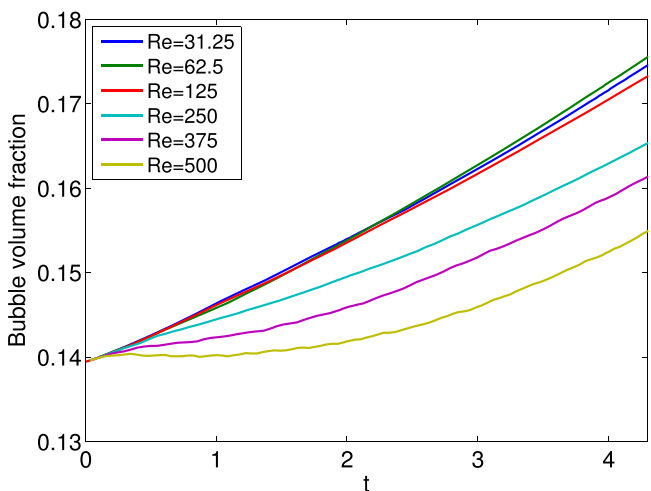


Fig. 14. The bubble growth for varying Re. The bubble volume fraction is in reference to the computational domain.

continues to become gentler but the peak turns around quickly to trend downward. At the wake of the bubble, the Nusselt number increases as the Re is increased until about $Re = 250$. At $Re = 250$, the Nusselt number for the bubble wake region is at the highest, after which it trends downwards as well. For $Re > 375$, the only rear half of the bubble or the liquid film seems to contribute to the jump in Nusselt number. For $Re > 500$, the largest Nusselt number distribution at the wall seems to have completely shifted from the tail of the bubble to the wake of the bubble, albeit both sides' Nusselt number diminishing. This indicates that beyond this point, the predictive models for boiling slug flow based on the film thickness are not valid. Also, note that for $Re > 500$ where there is continuous vortex shedding, the computational domain length can affect the Nusselt number distribution because the vortex can recirculate back to the bubble. For current research cases, the domain length has shown to have minor effect on the Nusselt number for the high Re cases due to the flattened out Nusselt number profiles. However, as the bubble grows further, the length of the computational domain will certainly need to increase as well.

In order to further investigate the large jump in Nusselt number as well as its decay at high Re, the temperature profiles for the reference case ($Re = 125$) and the $Re = 1000$ are compared in Fig. 11 (Top two) at the front of the bubble and in Fig. 11 (Bottom two) at the tail. First, it can be seen from the streamlines that there is a large recirculating region in front of the reference case bubble. The decay of Nusselt number near the bubble tip is attributed to this radial flow field. On the other hand, the case for $Re = 1000$ shows a much smaller recirculation region at the tip of the bubble due to the slicker shape of the bubble front. Thus, there is less decay of Nusselt number near the bubble tip.

Within the liquid film region, there are two main factors to the wall heat flux: the film thickness and the thermal boundary layer. As already been discussed, higher Re leads to thicker liquid film, thus lower Nusselt number at the wall. For the thermal boundary layer, higher Re results in higher liquid velocity around the bubble, which hinders the thermal boundary layer development and leads to a higher wall Nusselt number. Note that this is the opposite of the case in Mukherjee and Kandlikar [12], where the initial fluid temperature was set the same as the wall superheat temperature, whereas in current research, it is set at the saturation temperature. In turn, it can be said that the effect of the liquid film thickness dominates the thermal boundary layer effect on the Nusselt number for varying Re.

In Fig. 11, the peak of Nusselt number at the rear end corresponds to the highest crest of the interface for the reference case. A flow instability at the bubble's tail resulting in vortex shedding can be observed for the high Reynolds number case but it can be seen from Fig. 10 that its influence on Nu is limited at the quasi-steady state.

Fig. 12 shows the time evolution of the bubble shape and the temperature field for the $Re = 1000$ case. It shows that from the initial setup of the bubble, there is a startup effect causing a large recirculating region at the wake. Eventually, the initial effect dissipates and the bubble reaches its quasi-steady-state characteristic shape with the tail's oscillation continuously shedding vortices.

The space averaged Nusselt number for different Re is plotted against time in Fig. 13 (Top) along with the Nusselt number for pure liquid flow. Initially, the space averaged heat flux at the wall decays rapidly and slows down as the thermal boundary layer develops. It is interesting to see that the highest space averaged Nusselt number occurs for the reference case and there is no apparent order to the curves between $Re = 31.25$ to $Re = 375$. This result is in contrast to the monotonic decrease of Nusselt number at the front and at the liquid slug ahead of the bubble. Therefore, this behavior of space averaged Nusselt number can be attributed to the non-linear effect of the wavy shape of the bubble tail region and

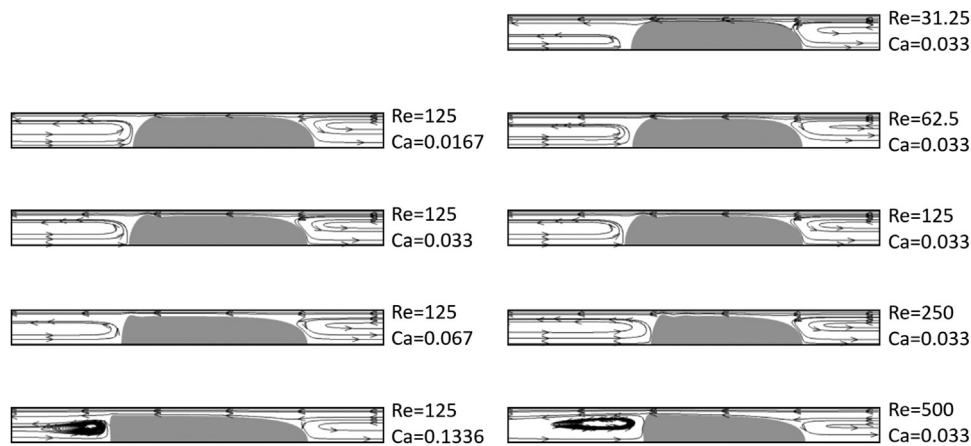


Fig. 15. Hydrodynamic characteristics of the Taylor bubble cases studied.

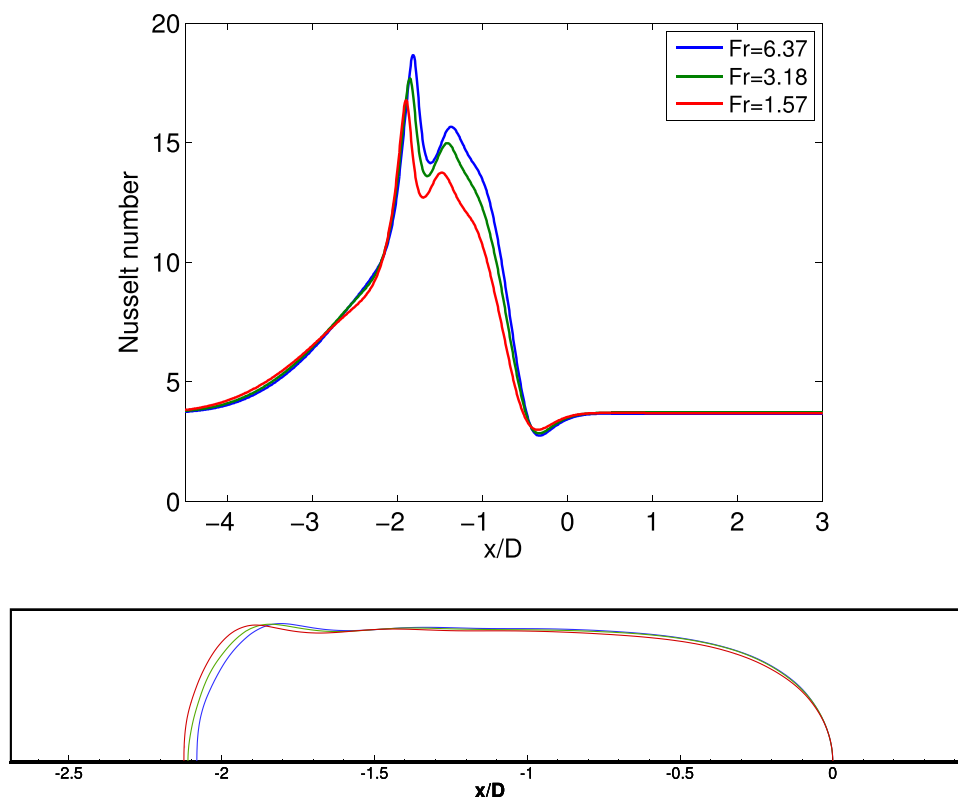


Fig. 16. (Top) Local Nusselt number distribution within the moving frame of reference and (Bottom) the bubble shape with Froude number varying in the range of 1.57–6.37. The time is at $t = 4$.

the oscillation of the bubble rear cap. Fig. 13 (Bottom) shows the longer time period of the Taylor bubble flow with phase change. It shows that the decay of space averaged Nusselt number becomes eventually overwhelmed by the bubble growth and the increase of thin film area.

Fig. 14 shows the bubble growth in time for varying Re . The bubble volume has been normalized with the total volume of the computational domain. The thin film thickness and the characteristic flow field of the low Re cases clearly contribute to a higher growth rate and the growth rate increases with time as the interface area increases.

In [41,42], three hydrodynamic characteristics of Taylor bubble flow have been categorized by the presence and the scale of the recirculating slug regions as well as the speed of the bubble with respect to the liquid slug. The conditions of the three cases have been correlated with the Re number and the Ca number. It is meaningful to identify these categories for a Taylor bubble flow because the convective mode of heat transfer in the liquid slug region can significantly vary for the different hydrodynamic characteristics. The hydrodynamic characteristics of the current research cases are shown in Fig. 15. It can be seen that our cases fall between Case B (where $Re = 100$, $Ca = 0.8$) and Case C (where $Re = 10$, $Ca = 0.03$) explained Fig. 1 of [42]. Our Ca numbers under consid-

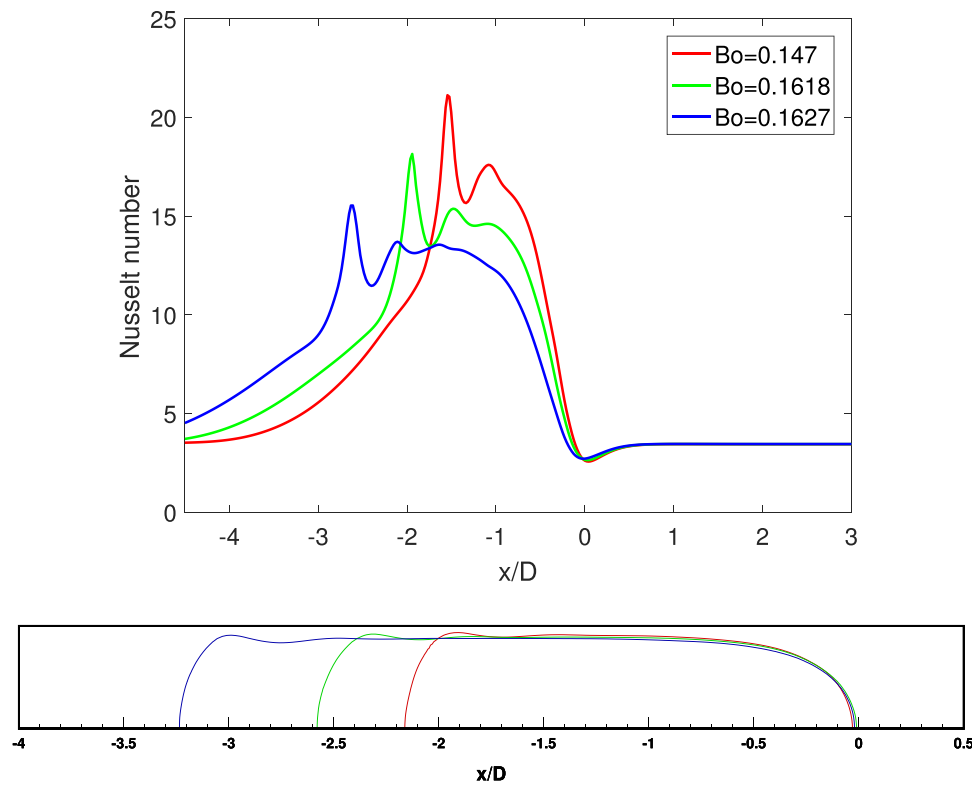


Fig. 17. (Top) Local Nusselt number distribution within the moving frame of reference and (Bottom) the bubble shape with Bond number varying in the range of 0.147–0.1627. The time is at $t = 4$.

eration are small from 0.0167 to 0.1336, close to Case C. Thus, our cases show slug recirculation at both the front and rear of the bubble. However, due to the higher Re number, the liquid film thickness is thicker and the bubble moves faster than the average liquid velocity as in case B. For cases with high Re number of 500 and high Ca number of 0.1336, they show closed liquid slug recirculation at the rear of the bubble as in case B. The local Nusselt number distributions with respect to the Froude number of half and one-fourth of the reference case is plotted in Fig. 16. The effect was found to be minor in comparison to the variations of capillary number and Reynolds number by the same factors but showed a clear effect of a decrease in the Nusselt number as the Froude number decreases due to increased film thickness. Another dimensionless number relevant to the slug flow regime is the Bond (or the Eötvös) number, where $Bo = \Delta\rho g L^2 / \sigma$. Previous researchers found that the significant difference between micro and macro channel flow is due to the large difference in the Bond number [41], and have proposed different Bond numbers, below which the gravitational effect is negligible, for instance $Bo = 3.37$ by Bretherton [36]. The Bond number in our study is 0.16 for the reference case, which falls clearly in the microchannel regime. However, there is potentially another aspect of the Bond number effect associated with flows involving phase change. For phase changing Taylor bubble flow, the Bond number affects the gas volume expansion rate and as a result, the Nusselt number as shown in Fig. 17. The isolated effect of the Bond number without altering the Ca number and the Re number can only be studied with variation of the gas density i.e., the liquid-gas density ratio, ρ' in Eq. (17). However, because the Bond number considers the density difference, not the density ratio, the bubble expansion rate does not scale proportionally with the Bond number. This can be seen in Fig. 17 that the slight increase of the Bond number can significantly increase the bubble expansion rate. The Nusselt number profile expands

as the bubble size increases but the amplitude is shown to decay.

3. Conclusions

A study on Taylor bubble flow with heat transfer and phase change in a vertical tube in axisymmetric coordinates has been carried out using the direct multiphase, phase change numerical method. The method incorporates continuous velocity and density fields within a thin interfacial region for accurate and numerically stable phase change phenomena while pertaining to sharp temperature and pressure jump conditions across the interface. A validation case was simulated and a good match was obtained with existing correlations. The influence of dimensionless parameters: the capillary number (Ca), the Reynolds number (Re), the Froude number (Fr) and the Bond number (Bo) on the local Nusselt number as well as other two-phase flow characteristics such as the bubble shape, the liquid film thickness and the bubble rise velocity have been investigated. In particular, the results showed that the thin liquid film is indeed the dominant heat transfer mechanism for small Re (<500) but beyond that point, the main mechanism has been identified as the flow at the bubble wake. The transition occurs due to the greater liquid film thickness and oscillations at the bubble tail as well as an increase in flow instability at a large value of the Reynolds number. The effect of the capillary number is shown to be monotonically analogous to its effect on the liquid film thickness. Consequently, the Nusselt number decreases with an increase in the capillary number. The Froude number has a relatively minor effect on film thickness and the Nusselt number while the Bond number increase leads to increase in bubble expansion rate.

Declaration of Competing Interest

The authors declare that they have no known competing financial interests or personal relationships that could have appeared to influence the work reported in this paper.

CRediT authorship contribution statement

Moon Soo Lee: Conceptualization, Methodology, Validation, Writing – original draft. **Amir Riaz:** Conceptualization, Methodology, Supervision, Writing – review & editing.

References

- [1] C. Horvath, B.A. Solomon, J.-M. Engasser, Measurement of radial transport in slug flow using enzyme tubes, *Ind. Eng. Chem. Fundam.* 12 (4) (1973) 431–439.
- [2] D. Oliver, A.Y. Hoon, 2-phase non-newtonian flow. 2. Heat transfer, *Trans. Inst. Chem. Eng. Chem. Eng.* 46 (4) (1968) T116.
- [3] J.A. Howard, P.A. Walsh, E.J. Walsh, Prandtl and capillary effects on heat transfer performance within laminar liquid-gas slug flows, *Int. J. Heat Mass Transf.* 54 (21) (2011) 4752–4761.
- [4] A. Majumder, B. Mehta, S. Khandekar, Local Nusselt number enhancement during gas-liquid Taylor bubble flow in a square mini-channel: an experimental study, *Int. J. Therm. Sci.* 66 (2013) 8–18.
- [5] K. Fukagata, N. Kasagi, P. Ua-arayaporn, T. Himeno, Numerical simulation of gas-liquid two-phase flow and convective heat transfer in a micro tube, *Int. J. Heat Fluid Flow* 28 (1) (2007) 72–82.
- [6] C. Narayanan, D. Lakehal, Two-phase convective heat transfer in miniature pipes under normal and microgravity conditions, *J. Heat Transf.* 130 (7) (2008) 074502.
- [7] Q. He, Y. Hasegawa, N. Kasagi, Heat transfer modelling of gas-liquid slug flow without phase change in a micro tube, *Int. J. Heat Fluid Flow* 31 (1) (2010) 126–136.
- [8] R. Gupta, D.F. Fletcher, B.S. Haynes, CFD modelling of flow and heat transfer in the Taylorflow regime, *Chem. Eng. Sci.* 65 (6) (2010) 2094–2107.
- [9] A.N. Asadolahi, R. Gupta, S.S. Leung, D.F. Fletcher, B.S. Haynes, Validation of a CFD model of Taylor flow hydrodynamics and heat transfer, *Chem. Eng. Sci.* 69 (1) (2012) 541–552.
- [10] A.A. Somasekhara Goud Sontti, CFD analysis of Taylor bubble in a co-flow microchannel with newtonian and non-newtonian liquid, *Ind. Eng. Chem. Res.* 56 (2017) 7401–7412.
- [11] T. Bandara, N.-T. Nguyen, G. Rosengarten, Slug flow heat transfer without phase change in microchannels: a review, *Chem. Eng. Sci.* 126 (2015) 283–295.
- [12] A. Mukherjee, S.G. Kandlikar, Numerical simulation of growth of a vapor bubble during flow boiling of water in a microchannel, *Microfluid. Nanofluidics* 1 (2) (2005) 137–145.
- [13] A. Mukherjee, Contribution of thin-film evaporation during flow boiling inside microchannels, *Int. J. Therm. Sci.* 48 (11) (2009) 2025–2035.
- [14] A. Mukherjee, S. Kandlikar, Z. Edel, Numerical study of bubble growth and wall heat transfer during flow boiling in a microchannel, *Int. J. Heat Mass Transf.* 54 (15) (2011) 3702–3718, doi:10.1016/j.ijheatmasstransfer.2011.01.030. <https://www.sciencedirect.com/science/article/pii/S0017931011001426>
- [15] Y. Zu, Y. Yan, S. Gedupudi, T. Karayiannis, D. Kenning, Confined bubble growth during flow boiling in a mini-/micro-channel of rectangular cross-section part II: approximate 3-d numerical simulation, *Int. J. Therm. Sci.* 50 (3) (2011) 267–273, doi:10.1016/j.ijthermalsci.2010.09.004. *Nano, Micro and Mini Channels*
- [16] R. Zhuang, W. Wang, Flow pattern of boiling in micro-channel by numerical simulation, *Int. J. Heat Mass Transf.* 55 (5) (2012) 1741–1753.
- [17] Y. Suh, W. Lee, G. Son, Bubble dynamics, flow, and heat transfer during flow boiling in parallel microchannels, *Numer. Heat Transf., Part A* 54 (4) (2008) 390–405.
- [18] M. Magnini, B. Pulvirenti, J.R. Thome, Numerical investigation of hydrodynamics and heat transfer of elongated bubbles during flow boiling in a microchannel, *Int. J. Heat Mass Transf.* 59 (2013) 451–471.
- [19] M.D. Zimmer, I.A. Bolotnov, Slug-to-churn vertical two-phase flow regime transition study using an interface tracking approach, *Int. J. Multiph. Flow* 115 (2019) 196–206, doi:10.1016/j.ijmultiphaseflow.2019.04.003. <https://www.sciencedirect.com/science/article/pii/S0301932218308942>
- [20] P. Junnosuke Okajima Stephan, Numerical simulation of liquid film formation and its heat transfer through vapor bubble expansion in a microchannel, *Int. J. Heat Mass Transf.* 136 (2019) 1241–1249.
- [21] J.H. Son, I.S. Park, Numerical simulation of phasechange heat transfer problems using heat fluxes on phase interface reconstructed by contour-based reconstruction algorithm, *Int. J. Heat Mass Transf.* 156 (2020) 119894, doi:10.1016/j.ijheatmasstransfer.2020.119894. <https://www.sciencedirect.com/science/article/pii/S0017931020306438>
- [22] J. Brackbill, D. Kothe, C. Zemach, A continuum method for modeling surface tension, *J. Comput. Phys.* 100 (1992) 335–354.
- [23] R. Gupta, D.F. Fletcher, B.S. Haynes, On the CFD modelling of Taylor flow in microchannels, *Chem. Eng. Sci.* 64 (12) (2009) 2941–2950.
- [24] M.S. Lee, A. Riaz, V. Aute, Direct numerical simulation of incompressible multiphase flow with phase change, *J. Comput. Phys.* 344 (2017) 381–418.
- [25] D.K. Agarwal, S.W.J. Welch, G. Biswas, F. Durst, Planar simulation of bubble growth in film boiling in near-critical water using a variant of the VOF method, *J. Heat Transf.* 126 (3) (2004) 329, doi:10.1115/1.1737779. <http://link.aip.org/link/JHTAO/v126/i3/p329/s1%26Agg=doi>
- [26] F. Gibou, L. Chen, D. Nguyen, S. Banerjee, A level set based sharp interface method for the multiphase incompressible Navier–Stokes equations with phase change, *J. Comput. Phys.* 222 (2) (2007) 536–555, doi:10.1016/j.jcp.2006.07.035. <http://linkinghub.elsevier.com/retrieve/pii/S0021999106003652>
- [27] S. Hardt, F. Wondra, Evaporation model for interfacial flows based on a continuum-field representation of the source terms, *J. Comput. Phys.* 227 (11) (2008) 5871–5895, doi:10.1016/j.jcp.2008.02.020. <http://linkinghub.elsevier.com/retrieve/pii/S0021999108001228>
- [28] D. Juric, G. Tryggvason, Computations of boiling flows, *Int. J. Multiph. Flow* 24 (3) (1998) 387–410, doi:10.1016/S0301-9322(97)00050-5. <http://linkinghub.elsevier.com/retrieve/pii/S0301932297000505>
- [29] G. Son, V. Dhir, Numerical simulation of saturated film boiling on a horizontal surface, *J. Heat Transf.* 119 (5) (1997) 25–54.
- [30] G. Tomar, G. Biswas, a. Sharma, a. Agrawal, Numerical simulation of bubble growth in film boiling using a coupled level-set and volume-of-fluid method, *Phys. Fluids* 17 (11) (2005) 112103, doi:10.1063/1.2136357. <http://link.aip.org/link/PHFLE6/v17/i11/p112103/s1%26Agg=doi>
- [31] M. Sussman, E. Fatemi, P. Smereka, S. Osher, An improved level set method for incompressible two-phase flows, *Comput. Fluids* 27 (5–6) (1998) 663–680, doi:10.1016/S0045-7930(97)00053-4. <http://linkinghub.elsevier.com/retrieve/pii/S0045793097000534>
- [32] M. Sussman, P. Smereka, S. Osher, A level set approach for computing solutions to incompressible two-phase flow, *J. Comput. Phys.* 114 (1) (1994) 146–159.
- [33] T. Taha, Z. Cui, Hydrodynamics of slug flow inside capillaries, *Chem. Eng. Sci.* 59 (6) (2004) 1181–1190.
- [34] D. Liu, S. Wang, Hydrodynamics of Taylor flow in noncircular capillaries, *Chem. Eng. Process.* 47 (12) (2008) 2098–2106, doi:10.1016/j.cep.2007.10.025. <https://www.sciencedirect.com/science/article/pii/S0255270107003571>
- [35] A.N. Asadolahi, R. Gupta, D.F. Fletcher, B.S. Haynes, Cfd approaches for the simulation of hydrodynamics and heat transfer in Taylor flow, *Chem. Eng. Sci.* 66 (22) (2011) 5575–5584, doi:10.1016/j.ces.2011.07.047. <https://www.sciencedirect.com/science/article/pii/S0009250911005185>
- [36] F. Bretherton, The motion of long bubbles in tubes, *J. Fluid Mech.* 10 (02) (1961) 166–188.
- [37] P. Aussillous, D. Quéré, Quick deposition of a fluid on the wall of a tube, *Phys. Fluids* (1994–Present) 12 (10) (2000) 2367–2371.
- [38] H. Liu, C.O. Vandu, R. Krishna, Hydrodynamics of Taylor flow in vertical capillaries: flow regimes, bubble rise velocity, liquid slug length, and pressure drop, *Ind. Eng. Chem. Res.* 44 (14) (2005) 4884–4897.
- [39] M.T. Kreutzer, F. Kapteijn, J.A. Moulijn, C.R. Kleijn, J.J. Heiszwolf, Inertial and interfacial effects on pressure drop of Taylor flow in capillaries, *AIChE J.* 51 (9) (2005) 2428–2440.
- [40] D. Lakehal, G. Larrignon, C. Narayanan, Computational heat transfer and two-phase flow topology in miniature tubes, *Microfluid. Nanofluidics* 4 (4) (2008) 261–271.
- [41] L.A.M. Rocha, J.M. Miranda, J.B.L.M. Campos, Wide range simulation study of Taylor bubbles in circular milli and microchannels, *Micromachines* 8 (5) (2017), doi:10.3390/mi8050154. <https://www.mdpi.com/2072-666X/8/5/154>
- [42] M.C. Silva, J.M. Miranda, J.B.L.M. Campos, J.P. Araújo, Mass transfer from a Taylor bubble to the surrounding flowing liquid at the micro-scale: a numerical approach, *Microfluid. Nanofluidics* 23 (2019) 1–21.